

# The influence of stacking fault energy on the microstructural and strain-hardening evolution of Fe–Mn–Al–Si steels during tensile deformation



D.T. Pierce<sup>a,\*</sup>, J.A. Jiménez<sup>b</sup>, J. Bentley<sup>c</sup>, D. Raabe<sup>d</sup>, J.E. Wittig<sup>e</sup>

<sup>a</sup> Advanced Steel Processing and Products Research Center, Colorado School of Mines, 1500 Illinois St., Golden, CO 80401, USA

<sup>b</sup> Centro Nacional de Investigaciones Metalúrgicas (CSIC), Avda. Gregorio del Amo, 8, 28040 Madrid, Spain

<sup>c</sup> Microscopy and Microanalytical Sciences, P.O. Box 7103, Oak Ridge, TN 37831-7103, USA

<sup>d</sup> Max-Planck-Institut für Eisenforschung, Max-Planck Str. 1, D-40237 Düsseldorf, Germany

<sup>e</sup> Vanderbilt University, PMB 351683, 2301 Vanderbilt Place, Nashville, TN 37232, USA

## ARTICLE INFO

### Article history:

Received 6 May 2015

Revised 4 August 2015

Accepted 14 August 2015

### Keywords:

TWIP steel

TRIP steel

Stacking-fault energy

Plasticity mechanisms

Twinning

## ABSTRACT

Understanding the relationship between the stacking-fault energy (SFE), deformation mechanisms, and strain-hardening behavior is important for alloying and design of high-Mn austenitic transformation- and twinning-induced plasticity (TRIP/TWIP) steels. The present study investigates the influence of SFE on the microstructural and strain-hardening evolution of three TRIP/TWIP alloys (Fe–22/25/28Mn–3Al–3Si wt.%). The SFE is increased by systemically increasing the Mn content from 22 to 28 wt.%. The Fe–22Mn–3Al–3Si alloy, with a SFE of  $15 \text{ mJ m}^{-2}$ , deforms by planar dislocation glide and strain-induced  $\epsilon_{\text{hcp}}/\alpha_{\text{bcc}}$ -martensite formation which occurs from the onset of plastic deformation, resulting in improved work-hardening at low strains but lower total elongation. With an increased SFE of  $21 \text{ mJ m}^{-2}$  in the Fe–25Mn–3Al–3Si alloy, both mechanical twinning and  $\epsilon_{\text{hcp}}$ -martensite formation are activated during deformation, and result in the largest elongation of the three alloys. A SFE of  $39 \text{ mJ m}^{-2}$  enables significant dislocation cross slip and suppresses  $\epsilon_{\text{hcp}}$ -martensite formation, causing reduced work-hardening during the early stages of deformation in the Fe–28Mn–3Al–3Si alloy while mechanical twinning begins to enhance the strain-hardening after approximately 10% strain. The increase in SFE from 15 to  $39 \text{ mJ m}^{-2}$  results in significant changes in the deformation mechanisms and, at low strains, decreased work-hardening, but has a relatively small influence on strength and ductility.

© 2015 Acta Materialia Inc. Published by Elsevier Ltd. All rights reserved.

## 1. Introduction

High-manganese transformation- and twinning-induced plasticity (TRIP/TWIP) steels are receiving significant research interest owing to their exceptional combination of strength, ductility and strain-hardening compared to existing steel [1–8]. These alloys show excellent promise for automotive applications as a means to reduce vehicle weight through downgauging and to enable room temperature (RT) forming of complex shaped parts. Typically, high-Mn TRIP/TWIP steels are metastable or stable austenite and besides high levels of Mn (18–30 wt.%) have additions of Al, Si, Cr, C and N [9–12]. The steels deform by a combination of dislocation glide and secondary deformation mechanisms such as  $\alpha_{\text{bcc}}/\epsilon_{\text{hcp}}$ -martensite formation and/or mechanical twinning [13].

The martensite platelets and mechanical twins act as planar obstacles and reduce the mean free path of dislocation glide. Dislocations pile up at interfaces between these planar defects and the matrix and cause significant back stresses [4] that impede the progress of similar dislocations. Back stresses contribute a significant amount to the flow stress (up to half the total flow stress in an Fe–22Mn–0.6C wt.% steel [14]). The shear displacements associated with martensite and mechanical twin formation are of secondary importance considering their direct contribution to the total strain [5,15]. However, the significant work-hardening caused by these planar defects delays local necking and results in large uniform elongations [1,5,16,17].

The activation of these secondary deformation mechanisms is controlled in part by the temperature- and composition-dependent stacking-fault energy (SFE). With decreasing SFE, the plasticity mechanisms change from (i) dislocation glide to (ii) dislocation glide and mechanical twinning to (iii) dislocation glide

\* Corresponding author.

E-mail address: [dpierce@mines.edu](mailto:dpierce@mines.edu) (D.T. Pierce).

and  $\gamma_{\text{fcc}} \rightarrow \epsilon_{\text{hcp}}$  martensitic transformations [3,18–23]. In addition,  $\epsilon_{\text{hcp}}$ -martensite can act as nucleation sites for the formation of  $\alpha_{\text{bcc}}$ -martensite [23]. Linking SFE values with specific plasticity mechanisms is important since each deformation mode may alter the mechanical properties or result in deleterious effects. For instance, the suppression of  $\epsilon_{\text{hcp}}$ -martensite may reduce the susceptibility to hydrogen embrittlement [24–26] and dynamic strain aging (DSA) in some TRIP/TWIP steels [27–29].

Most investigations on the relationship between SFE, deformation mechanisms, and mechanical properties rely on thermodynamic models to calculate the temperature- and composition-dependent SFE [3,12,18,20,22]. Thermodynamic SFE calculations for Fe–Mn based TRIP and TWIP steels typically assume two atomic planes of hcp<sup>1</sup> stacking (intrinsic stacking fault) separated from the austenite matrix by two interfaces [3,12,19,20,30,31]. Allain et al. [20] compared the thermodynamically calculated SFE, deformation mechanisms, and tensile properties of an Fe–22Mn–0.6C wt.% steel at –196 °C, RT and 400 °C. The authors reported the deformation mechanisms changed with increasing temperature and SFE from dislocation glide and  $\epsilon$ -martensite formation (SFE  $\sim 10 \text{ mJ m}^{-2}$ ), to dislocation glide and mechanical twinning (SFE  $\sim 19 \text{ mJ m}^{-2}$ ) to only dislocation glide (SFE  $\sim 80 \text{ mJ m}^{-2}$ ). Other temperature-sensitive phenomena such as thermally activated dislocation dynamics [32] and DSA [6] may obscure the influence of a change in SFE on the microstructure and mechanical properties. Additionally, as previously pointed out [18], several sources of uncertainty arise from using thermodynamic SFE models including: (1) thermodynamic parameters for the same elements that differ depending on author (e.g., [3,12,18,22,33]), (2) the austenite/ $\epsilon_{\text{hcp}}$ -martensite interfacial energy is typically the largest contribution to the SFE at RT [18], is the most challenging to determine [16,34], and exhibits significant variation with composition and temperature [12,18,35] and (3) the strain energy associated with contraction of the molar volume during the fcc to  $\epsilon_{\text{hcp}}$ -martensite phase ranges from 1 to  $7 \text{ mJ m}^{-2}$  [18,35] and is sometimes neglected in thermodynamic SFE calculations [12,20]. Also, Suzuki type effects are usually neglected in such calculations. This effect refers to a situation where the solute concentration at the stacking fault may differ from that of the bulk alloy surrounding it due to partitioning and also due to the effects of the abutting partial dislocations.

Direct experimental measurements of the SFE avoid the aforementioned uncertainties [10,11,18,36,37]. Jeong et al. [11] measured the SFE of Fe–18Mn–0.6C, Fe–18Mn–0.6C–1.5Si and Fe–18Mn–0.6C–1.5Al alloys indirectly by XRD line profile analysis, reporting values of  $19.3 \pm 2.5$ ,  $13.8 \pm 2.5$  and  $29.1 \text{ mJ m}^{-2}$ , respectively. No martensite formation was detected by XRD and additions of Al and Si both decreased the elongation, while reducing and increasing the UTS, respectively. Kim et al. [10] measured SFEs of  $13 \pm 3$  and  $30 \pm 10 \text{ mJ m}^{-2}$  by measurement of partial dislocation separation for Fe–18Mn–0.6C and Fe–18Mn–0.6C–1.5Al alloys, respectively. The authors showed that Al additions increase the SFE, reduce work-hardening and ductility, while delaying the onset of DSA. Their SFE measurements assumed isotropic elasticity and no distinction between the separation of two partial-dislocation images and separation of the cores is made, which can cause additional uncertainty in the SFE values [18]. In addition, the value of SFE corresponding to the transition from  $\epsilon_{\text{hcp}}$ -martensite to mechanical twinning is not shown in the studies by Jeong et al. [11] or Kim et al. [10]. Finally, the large solid-solution strengthening coefficients of Al and Si [4,6,11,28], relative to Mn [6], make it difficult to de-convolute the influence of

the SFE on mechanical properties from the above-mentioned studies.

The present study uses three Fe–22/25/28Mn–3Al–3Si model alloys with low C content ( $<0.01 \text{ wt.}\%$ ) to investigate the effect of changes in SFE on the RT microstructural evolution and mechanical properties during tensile deformation. The SFEs were previously measured by analysis of partial-dislocation separations using weak-beam dark-field (WBDF) TEM [18]. The accuracy of the SFE measurements was improved by incorporating: (1) elastic anisotropy determined from polycrystalline specimens using a novel nanoindentation method [38], (2) a correction between the actual and observed partial dislocation spacing [18], and (3) dislocation core thickness effects [18]. The RT SFEs of the Fe–22/25/28Mn–3Al–3Si alloys increase from  $15 \pm 3$ , to  $21 \pm 3$ , to  $39 \pm 5 \text{ mJ m}^{-2}$ , respectively, by the systematic increase in the Mn content while keeping the amount of all other alloying additions approximately constant. Dislocation mobility, or the ease of which dislocations can move through the structure, significantly influences the work-hardening behavior and flow stress of high-Mn TRIP/TWIP steels and is referred to throughout the manuscript. Reducing dislocation mobility can occur, for instance, by: (1) grain size refinement [4,14], (2) solid solution strengthening [11,28], (3) reducing the ability for partial dislocations to recombine and cross slip to planes more favorably oriented for slip or to overcome obstacles [4], and (4) the formation of planar defects (e.g.,  $\epsilon_{\text{hcp}}$ -martensite martensite laths and mechanical twins) or dislocation structures [9] which reduce the mean free path of dislocation glide, result in dislocation pile ups, and lead to back stresses [14]. The grain size of each alloy is approximately  $21 \mu\text{m}$  and changes in dislocation mobility due to grain size differences are insignificant. The solid-solution hardening coefficients of Mn for yield and UTS are small [6] indicating that this contribution to changes in dislocation mobility is minor. The ability of two partial dislocations to recombine and cross slip onto a more favorable slip plane is primarily governed by the SFE and the friction stress [39]. The friction stress is similar in the present materials, suggesting the propensity for cross slip is primarily controlled by the SFE. Changes in the type and extent of secondary deformation mechanisms in the present steels during RT deformation will also be primarily governed by the SFE, as described above. Consequently, changes in the dislocation mobility, the microstructural evolution during deformation, and the mechanical properties of the three alloys in the present study can be primarily attributed to differences in the SFE. Quasi-static strain rates and sub-sized tensile specimens are employed in order to reduce adiabatic heating and minimize the resulting SFE increase during tensile deformation. Tensile tests were interrupted at specific levels of plastic true strain to observe the development of the deformation microstructures using optical microscopy (OM), X-ray diffraction (XRD) and transmission electron microscopy (TEM).

## 2. Materials

Three Fe–22/25/28Mn–3Al–3Si wt.% alloys were induction melted in an argon atmosphere and cast into ingots. As-cast ingots were thermo-mechanically processed by hot rolling at  $1100 \text{ }^{\circ}\text{C}$  to produce strips of 3 mm thickness which were subsequently cold rolled to 1.5 mm thickness. The resulting sheet was recrystallized at  $900 \text{ }^{\circ}\text{C}$  for 30 min yielding a microstructure with equiaxed grains of  $\sim 21 \mu\text{m}$  in diameter for each composition. Sub-sized flat tensile specimens with a 20 mm gauge length and 5 mm width were cut from the sheet in the direction parallel to the rolling direction using electro-discharge machining (EDM). The compositions, difference in Gibbs free energy of the fcc to hcp phases,  $\Delta G_{\text{fcc} \rightarrow \text{hcp}}$  [18], and SFE are listed in Table 1.

<sup>1</sup> More correctly it is hexagonal, but hcp finds general use in the literature and will be used here for convenience.

**Table 1**Chemical compositions of the steels in wt.% unless otherwise specified,  $\Delta G^{\text{fcc} \rightarrow \text{hcp}}$  [18], and SFE [18].

Designation	Material	Mn	Al	Si	C	O (ppm)	Fe	$\Delta G^{\text{fcc} \rightarrow \text{hcp}}$ (J mol <sup>-1</sup> ) [18]	SFE (mJ m <sup>-2</sup> ) [18]
22%Mn	Fe–22Mn–3Al–3Si	22.2	2.76	2.92	0.0093	<5	Bal.	–88	15
25%Mn	Fe–25Mn–3Al–3Si	24.7	2.66	2.95	0.0053	<5	Bal.	31	21
28%Mn	Fe–28Mn–3Al–3Si	27.5	2.74	2.89	0.0071	<5	Bal.	199	39

### 3. Experimental procedure

Specimens of the 22, 25 and 28%Mn alloys were strained in tension at a rate of  $4 \times 10^{-4} \text{ s}^{-1}$  and were interrupted at 0.03, 0.1, 0.18, 0.34, 0.44 and 0.47 plastic true strain to characterize the development of the deformation microstructures using optical microscopy (OM), X-ray diffraction (XRD) and transmission electron microscopy (TEM). Specimens for OM were prepared by standard metallographic procedures, with an automatic polishing system. Low loads were used during this process, and successively decreased from 25 to 10 N for the final polish. The final polish utilized a suspension of 0.05  $\mu\text{m}$  colloidal silica for chemical–mechanical polishing to ensure a flat surface with minimal deformation induced from the polishing process. A 10% Nital solution was used to etch the polished specimens.

Measurements of phase volume fractions utilized a Bruker AXS D8 X-ray diffractometer equipped with a Co X-ray tube (using the  $K_{\alpha 1}$  wavelength), Goebel mirror optics and a LynxEye Linear Position Sensitive Detector for ultra-fast XRD measurements. A current of 30 mA and a voltage of 40 kV were employed as tube settings. The XRD data were collected over a  $2\theta$  range of 30–120° with a step size of 0.02°. For the application of the Rietveld refinement, instrument functions were empirically parameterised from the profile shape analysis measured under the same conditions for an AISI Type 316 stainless steel standard prepared by hot isostatic pressing. This study used version 4.2 of the Rietveld analysis program TOPAS (Bruker AXS) for the XRD data refinement. The room-temperature structures used in the refinement were ferrite, austenite and  $\epsilon_{\text{hcp}}$ -iron.

For TEM, disks 3 mm in diameter were cut from the gauge length of specimens deformed to 0.03, 0.1, 0.18 and 0.34 true strain using EDM. The 3-mm disks were mechanically polished to  $\sim 100 \mu\text{m}$  thickness and then jet electro-polished to electron transparency with a TenuPol-5 using a solution of 70% methanol and 30% nitric acid at  $-30^\circ\text{C}$ . Microstructures were analyzed with a Philips CM20T TEM operating at 200 kV and equipped with an Advanced Microscopy Techniques XR42HTV charge-coupled device (CCD) camera.

## 4. Results

### 4.1. X-ray diffraction

Analysis of XRD data for the volumes of different phases reveals a small amount of ferrite (<1%) in the undeformed microstructure and  $\epsilon$ - and  $\alpha$ -martensite in the deformed microstructures of the 22%Mn alloy. The analysis also indicates the 25 and 28%Mn alloys are fully austenitic before and after deformation. The fractions, estimated rate of transformation of austenite to martensite, and rates of formation of  $\epsilon$ - and  $\alpha$ -martensite, as a function of true strain are shown in Fig. 1 for the 22%Mn alloy. The rates of transformation/formation are the derivatives of a polynomial fit to the phase volume vs. true strain data. The rate of formation of  $\epsilon$ -martensite is greater than that of  $\alpha$ -martensite from 0 to 0.1 true strain, consistent with a previous report that  $\epsilon$ -martensite is often a precursor to  $\alpha$ -martensite formation in TRIP steels [23]. The rate

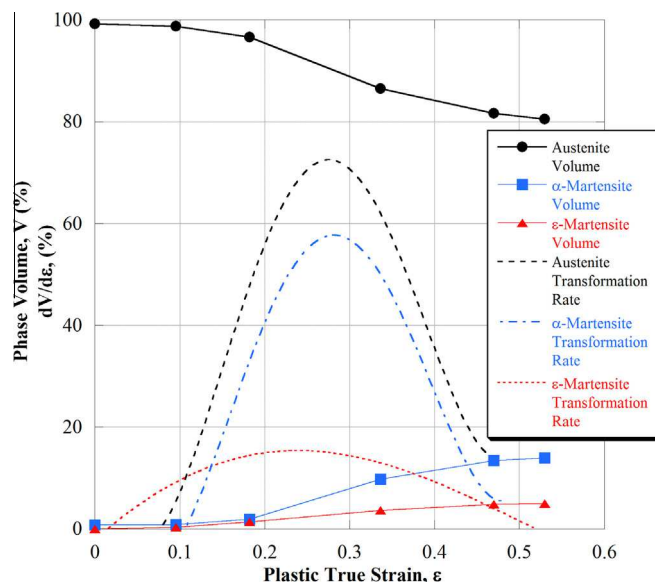


**Fig. 1.** Phase volume % (solid lines) and estimated transformation rates (broken lines) of austenite,  $\epsilon_{\text{hcp}}$ -martensite and  $\alpha$ -martensite vs. plastic true strain for the 22%Mn alloy.

of austenite to martensite transformation is large from 0.18 to 0.34 true strain, exhibiting an apparent maximum near 0.27 true strain.

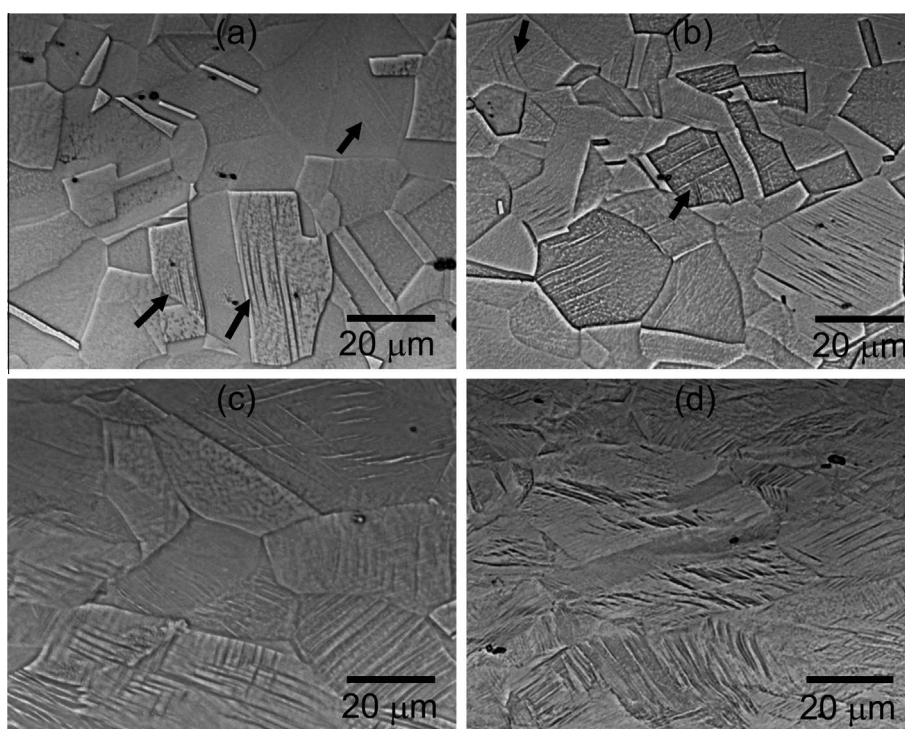
### 4.2. Optical microscopy

Fig. 2 shows optical micrographs of the 25%Mn alloy after deformation of 0.1, 0.18, 0.34 and 0.56 true strain (maximum uniform elongation). The tensile axis corresponds to the horizontal direction of each micrograph. The etched samples reveal planar secondary deformation structures such as bundles of mechanical twins and/or  $\epsilon_{\text{hcp}}$ -martensite laths (both occur in the 25%Mn alloy as shown in Section 4.4 below). After 0.1 true strain (Fig. 2a) mechanical twins and/or  $\epsilon_{\text{hcp}}$ -martensite laths (TEM or electron backscatter diffraction (EBSD) is required to differentiate) are evident in only a small percentage of grains. After 0.18 true strain (Fig. 2b) most grains show evidence of primary (occurring in only one system) mechanical twinning and/or  $\epsilon_{\text{hcp}}$ -martensite lath formation whereas a few grains begin to show evidence of secondary deformation structures in two or more variants (indicated by arrows). After 0.34 true strain (Fig. 2c) nearly all grains exhibit secondary deformation mechanisms in multiple orientations and these features are distributed uniformly over the entire grain surface. At maximum uniform elongation (Fig. 2d) the microstructure consists of elongated grains. Significant curvature of the slip bands indicates a high degree of intra-granular lattice misorientation.

### 4.3. TEM – 0.03 true strain

After 0.03 true strain, the microstructure of the 22%Mn alloy exhibits a planar dislocation structure of partial dislocations and large stacking faults typically activated in two slip systems. The stacking faults ranged in width (separation distance between the





**Fig. 2.** Optical micrographs of the 25%Mn alloy deformed to (a) 0.1 (mechanical twins and  $\epsilon_{\text{hcp}}$ -martensite laths are indicated by arrows), (b) 0.18 (mechanical twins and  $\epsilon_{\text{hcp}}$ -martensite laths in multiple slip systems are indicated by arrows), (c) 0.34 and (d) 0.55 true strain. The tensile axis is in the horizontal direction.

Shockley partials) from 100 nm to 2  $\mu\text{m}$ , approximately two orders of magnitude greater than the equilibrium separation of 5 to 12 nm as determined previously [18]. In Fig. 3a, a grain with numerous stacking faults after 0.03 true strain is shown. Many of these large faults may well be nascent or embryonic  $\epsilon_{\text{hcp}}$ -martensite laths [40,41]. Fig. 3b was recorded near a  $[110]$  zone and shows the leading partials of stacking faults on  $(111)$  or  $(-1-11)$  type plane impinging on slip bands or  $\epsilon_{\text{hcp}}$ -martensite laths on  $(1-11)$ . The arrows indicate locations where the  $\epsilon_{\text{hcp}}$ -martensite laths are blocking the glide of partial dislocations. As shown in Fig. 3c, the microstructure of the 25% Mn alloy after deformation to 0.03 true strain contains stacking faults with widths (distance between partial dislocations) that are significantly smaller than those observed in the 22%Mn alloy. Constricted dislocations displaying curvature or waviness are also evident in Fig. 3c. In Fig. 3d, the microstructure of the 28%Mn alloy after 0.03 true strain consists of isolated dislocations and localized areas of tangles of higher dislocation density. The majority of dislocations appear to be constricted when viewed in the bright-field (BF) imaging mode.

#### 4.4. TEM – 0.1 true strain

After 0.1 true strain, the microstructure of the 22%Mn alloy exhibits a planar dislocation structure with larger irregularly spaced and overlapping stacking faults, as shown in Fig. 4a, and more well-developed  $\epsilon_{\text{hcp}}$ -martensite lath structures, like those in Fig. 4b. In fact, it is likely that the overlapping faults, such as in Fig. 4a, are the broad faces of highly inclined  $\epsilon_{\text{hcp}}$ -martensite laths, which if tilted to be on edge would appear similar to those in Fig. 4b. The lath structures in Fig. 4b have the  $\{111\}_{\gamma} \parallel \{0001\}_{\epsilon} / (1-10)_{\gamma} \parallel (1-210)_{\epsilon}$  orientation relationship on two separate slip systems intersecting one another, as the inset selected area diffraction (SAD) pattern clearly reveals. In Fig. 4b, the apparent thickness of the  $\epsilon_{\text{hcp}}$ -martensite laths is greater than those observed at 0.03 true strain in Fig. 3b. Also in Fig. 4b, some laths intersect each other (indicated by black arrows) while others terminate at the interface

of  $\epsilon_{\text{hcp}}$ -martensite laths on non-coplanar slip systems (indicated by white arrows). In a survey of twenty grains from multiple TEM samples, 45% of grains contained well-developed (structure identifiable by SAD)  $\epsilon_{\text{hcp}}$ -martensite lath structures whereas none contained evidence of mechanical twinning (see Table 2). The other 55% of grains contained large stacking faults but no characteristic  $\epsilon_{\text{hcp}}$ -martensite reflections were observed in SAD patterns recorded at either  $\langle 111 \rangle_{\gamma}$  or  $\langle 110 \rangle_{\gamma}$  zone axes of the matrix. The absence of characteristic  $\epsilon_{\text{hcp}}$ -martensite reflections may arise because the laths were too thin or the volume fraction was too low, possibly due to a Schmid factor effect or specific stress states on the leading and trailing Shockley partials, which may occur for some grain orientations relative to the tensile axis that could limit the extension of the stacking faults.

The microstructure of the 25%Mn alloy after 0.1 true strain is dominated by planar features and contains a high density of stacking faults with separations between partial dislocations much less than those observed in the 22%Mn alloy. Unlike in the 22%Mn alloy, mechanical twinning is the dominant secondary deformation mechanism while  $\epsilon_{\text{hcp}}$ -martensite is also present but in smaller amounts. In a survey of twenty grains, 20% exhibited mechanical twinning and 10% showed  $\epsilon_{\text{hcp}}$ -martensite lath structures (Table 2). Fig. 5a and b show the microstructures imaged near a  $\langle 110 \rangle$  zone axis. Fig. 5a shows a dislocation network between mechanical twins and Fig. 5b shows  $\epsilon_{\text{hcp}}$ -martensite laths occurring mostly in one variant with fine inter-lath spacing ( $\sim 50$  nm). However, the inset SAD in Fig. 5b is shown on an expanded scale in Fig. 5c and faint twin reflections are also observed in addition to the more intense matrix and  $\epsilon_{\text{hcp}}$ -martensite reflections, suggesting that for the region shown in Fig. 5b  $\epsilon_{\text{hcp}}$ -martensite and small amounts of mechanical twinning are occurring on the same matrix habit plane. Twins are easily distinguishable from  $\epsilon_{\text{hcp}}$ -martensite laths in  $\langle 110 \rangle$  zone SAD patterns; twins give rise to extra reflections at the one-third positions along  $\langle 111 \rangle$  rows except through the central spot, whereas the extra reflections produced by  $\epsilon_{\text{hcp}}$ -martensite, although also along  $\langle 111 \rangle$  rows, are based on a

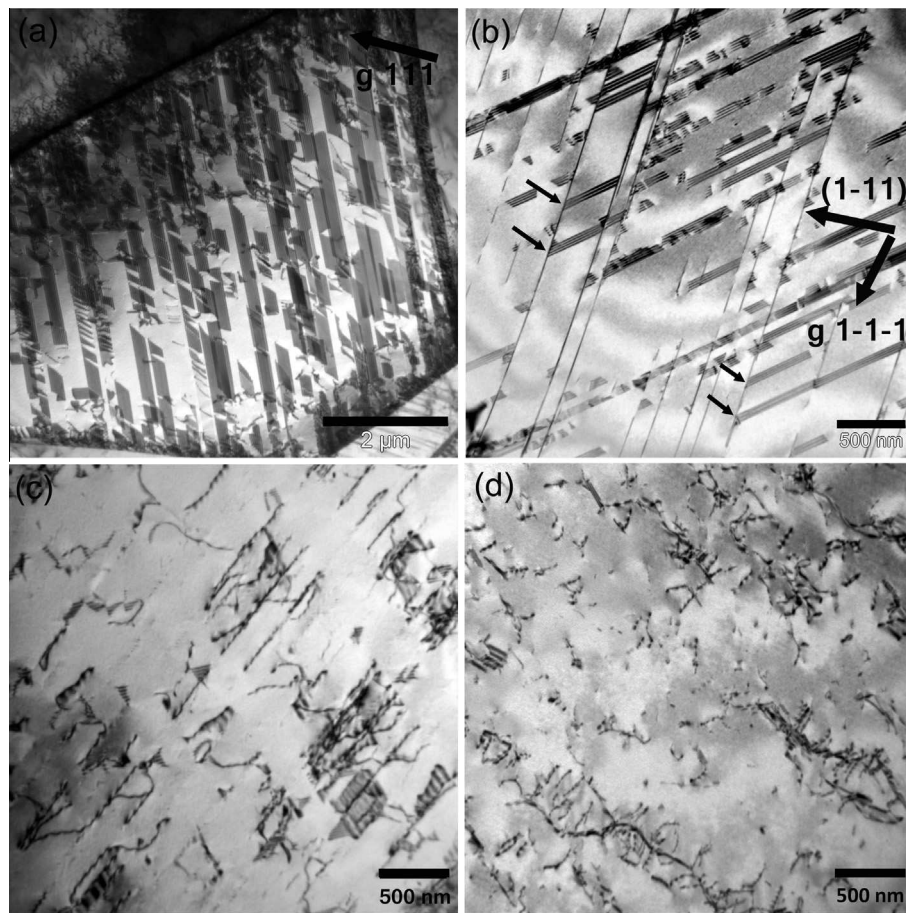


**Fig. 3.** BF TEM micrographs after 0.03 plastic true strain. (a) The microstructure of a grain in the 22%Mn alloy exhibiting large stacking faults on two slip systems. (b) Image of the microstructure in the 22%Mn alloy obtained with a beam direction near  $[1\ 1\ 0]$  using a  $1\ -1\ -1$  diffracting ( $g$ )-vector. (c) Grain exhibiting a defect structure with both planar and wavy characteristics in the 25%Mn alloy. (d) Image of the microstructure in the 28%Mn alloy showing wavy dislocations with localized areas of dislocation tangles.

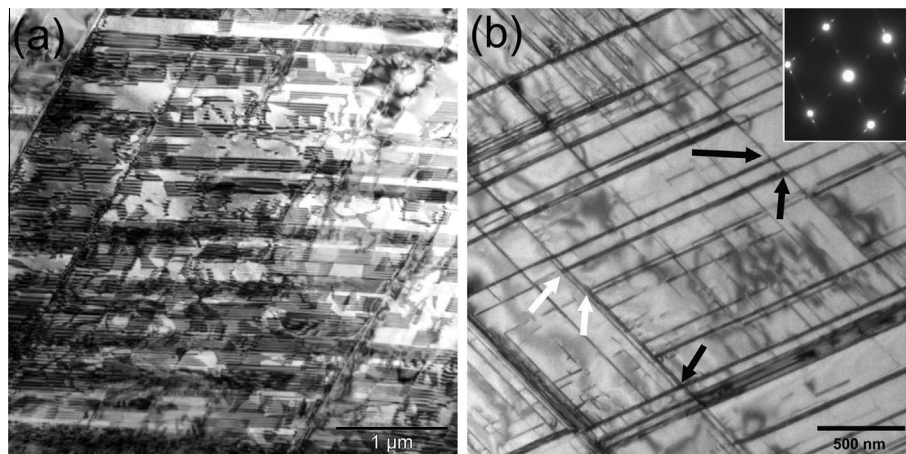


**Fig. 4.** TEM BF images of the 22%Mn alloy after 0.1 plastic true strain. (a) A grain with a high density of large overlapping SFs and (b) a grain exhibiting  $\epsilon_{\text{hcp}}$ -martensite laths in two edge-on variants. The SAD pattern (inset) was recorded at the  $[1\ 1\ 0]$  zone and exhibits characteristic  $\epsilon_{\text{hcp}}$ -martensite diffraction spots while the BF image was taken slightly off the zone axis in a two-beam condition. Arrows identify lath intersections (black) or where one lath terminates at another non-coplanar lath (white).

rectangular net with the short side corresponding to the forbidden but doubly diffracted  $(0001)_\epsilon$  at approximately the one-half  $(1\ 1\ 1)$  position of the matrix (i.e. on the row through the central spot). Multiple variants complicate the patterns, but double diffraction effects between the planar defects and the matrix are minimal for these edge-on interfaces [42]. The TEM observations are in

agreement with optical microscopy (Fig. 2a) and indicate that the majority of grains have not developed secondary deformation structures after 0.1 true strain in the 25%Mn alloy.

The microstructure of the 28%Mn alloy after 0.1 true strain exhibited a variety of different characteristics. Fig. 6a depicts a grain exhibiting dislocation cells (DCs) where areas  $\sim 1\ \mu\text{m}$  wide



**Table 2**

Percentage of grains after 0.1 and 0.18 true strain containing well-developed  $\epsilon_{\text{hcp}}$ -martensite or mechanical twinning.

True strain	Secondary deformation mechanism	Material		
		22% Mn	25% Mn	28% Mn
0.1	$\epsilon_{\text{hcp}}$ -martensite	45%	10%	0%
	Mechanical twinning	0%	20%	25%
0.18	$\epsilon_{\text{hcp}}$ -martensite	100%	36%	0%
	Mechanical twinning	0%	79%*	100%

\* Some grains contained both mechanical twinning and  $\epsilon_{\text{hcp}}$ -martensite.

have low dislocation density and are surrounded by cell walls of higher dislocation density. In contrast, Fig. 6b shows the microstructure of a grain with extensive mechanical twinning. The dark-field (DF) image in Fig. 6b is formed using the  $\{111\}$  twin reflection as depicted in the inset SAD pattern and shows fine mechanical twins with an average thickness of  $\sim 20$  nm. Mechanical twinning that could be identified by SAD was present in 25% of grains but none showed evidence of  $\epsilon_{\text{hcp}}$ -martensite (see Table 2). The different microstructures observed (DCs vs. mechanical twinning) are consistent with other reports of a strong relationship between grain orientation and deformation mechanism in high-Mn steels with medium SFEs [2,9,17].

#### 4.5. TEM – 0.18 true strain

After 0.18 true strain, nearly all grains in the 22%Mn alloy display significant grain refinement from  $\epsilon_{\text{hcp}}$ -martensite lath structures. Fig. 7a depicts a grain with a fine  $\epsilon_{\text{hcp}}$ -martensite lath structure. Mechanical twinning continues to be suppressed in the 22%Mn alloy at this strain. The 25%Mn alloy after 0.18 true strain showed  $\epsilon_{\text{hcp}}$ -martensite laths and mechanical twinning in approximately the same proportion as after 0.1 true strain (see Table 2). Nearly all grains in the 28%Mn alloy exhibit mechanical twinning after 0.18 true strain and the first development of twinning in two variants is observed (e.g., Fig. 7b). Both variants of mechanical twins exhibit evidence of being sheared. Observation of the matrix-twin interface of both twin variants reveals significant dislocation accumulation.

#### 4.6. TEM – 0.34 true strain

The microstructures show extensive grain refinement from secondary deformation structures after 0.34 true strain in all three

steels. Secondary deformation structures exist in two or more variants in nearly all grains. In the 22%Mn alloy,  $\alpha_{\text{bcc}}/\epsilon_{\text{hcp}}$ -martensite are the dominant secondary deformation mechanisms but mechanical twins also form at this strain as illustrated in Fig. 8a. High densities of trapped dislocations are observed between the mechanical twins in Fig. 8a. In the 28%Mn alloy, a refined microstructure consisting of mechanical twins in two variants is present after deformation to 0.34 true strain, also containing a high dislocation density between parallel mechanical twins. In several areas in Fig. 8b the mechanical twins are bowed indicating a high degree of intra-granular lattice misorientation and residual stress. Although not shown here, both mechanical twinning and  $\epsilon_{\text{hcp}}$ -martensite were observed in the 25%Mn alloy, sometimes in as many as three different variants in a single grain, with a high density of dislocations trapped between the planar defects.

#### 4.7. Strain-hardening behavior

The true stress and strain-hardening rates vs. true strain are presented in Fig. 9a and b, respectively. Each curve terminates at maximum uniform elongation. The Fe-22/25/28Mn-3Al-3Si steels exhibit an excellent combination of strength and ductility owing to intense strain-hardening. Three tensile tests performed for each composition show excellent reproducibility and no evidence of DSA. The flow stress of the 22%Mn alloy is on average about 70 MPa greater than that of the 25 and 28%Mn alloys.

Fig. 9b displays the normalized strain-hardening rate,  $(d\sigma/d\epsilon)/G$ , where  $G$  is the experimental (ultrasonic pulse echo) shear modulus of 69 GPa [43], vs. true strain for the 22, 25 and 28%Mn alloys. The strain-hardening rates are the derivatives of 9th order polynomials functions fitted to the true stress vs. true strain curves. Multi-stage work-hardening behavior, which is common in low SFE alloys that exhibit secondary deformation mechanisms [2,4,9,44], is observed in all three alloys. The strain hardening rates decrease monotonically until failure. The 22%Mn alloy shows six distinct stages of strain-hardening (stage 2 is subdivided into a–c) and the 25 and 28%Mn alloys four stages. The stages of strain-hardening described here do not correspond to the classical work-hardening stages of single- and polycrystals [45,46]. The 22%Mn alloy exhibits substantially greater strain-hardening rates in stages 1 and 2 as shown in Fig. 9b and inset. All three alloys exhibit nearly identical strain-hardening rates in stage 3 ( $\sim 0.34$  to 0.5 true strain) which decrease from  $\sim 0.022$  to 0.019. Stage 4 is characterized by an abrupt decrease in strain-hardening for each alloy, which occurs at slightly larger strains in the 25 and 28%Mn alloys, just before maximum uniform elongation. The maximum increase

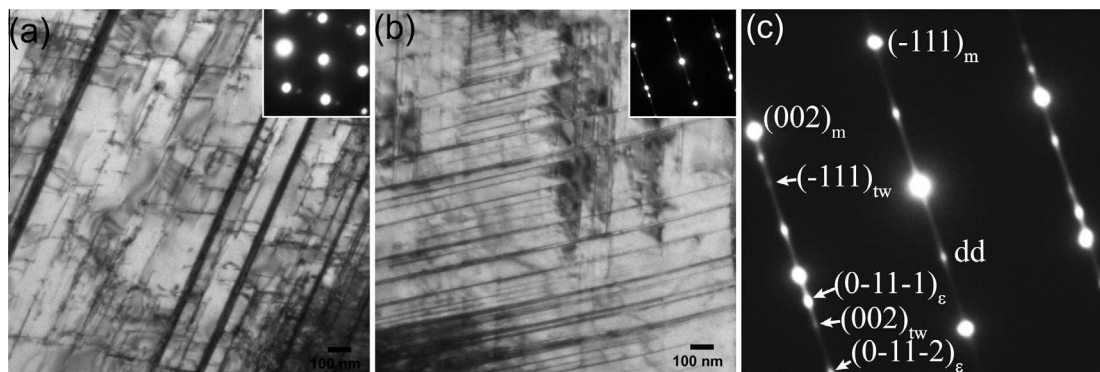


**Fig. 5.** 25%Mn alloy deformed to 0.1 true strain. BF images of (a) mechanical twinning and (b) fine  $\epsilon_{\text{hcp}}$ -martensite lath structure with the  $(111)_{\gamma} \parallel (0001)_{\epsilon} \parallel [1-10]_{\gamma} \parallel [1-210]_{\epsilon}$  orientation relationship. The SAD patterns were recorded at a  $[110]$  beam direction for identification of secondary deformation structures whereas the BF images were recorded a few degrees off axis in two beam conditions. The inset SAD pattern in (b) is shown on an expanded scale in (c) and faint twin reflections (tw) are observed in addition to the more intense matrix (m) and  $\epsilon_{\text{hcp}}$ -martensite ( $\epsilon$ ) reflections. The reflection labeled dd is due to double diffraction between the  $\{0-11-1\}_{\epsilon}$  and  $\{01-10\}_{\epsilon}$  reflections and similar paths.

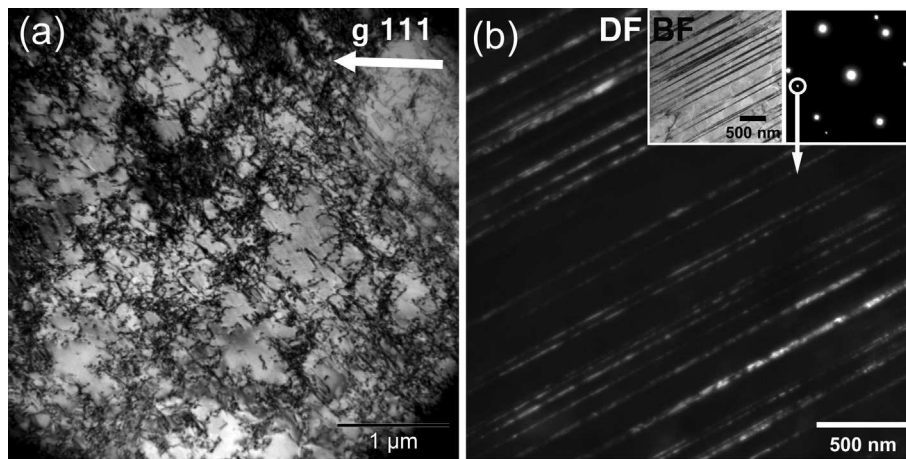


**Fig. 6.** TEM Images of the microstructure in the 28%Mn alloy after 0.1 true strain. (a) BF image of a grain with a dislocation cell structure. (b) DF image of mechanical twins using the {111} twin refraction. The SAD pattern and BF image (insets) were recorded from the [011] zone and slightly off axis in a two-beam condition, respectively.

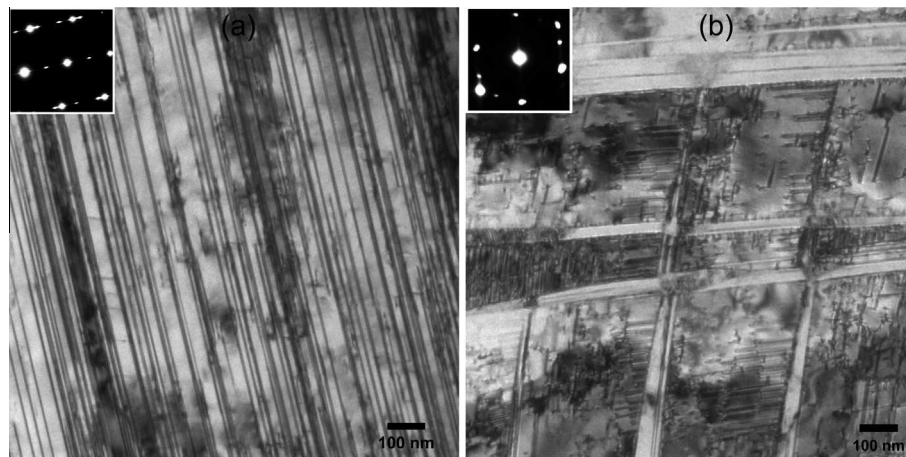


**Fig. 7.** TEM BF micrographs after deformation to 0.18 true strain showing in (a) in the 22%Mn alloy, a fine  $\epsilon_{\text{hcp}}$ -martensite lath structure with the  $(111)_{\gamma} || (0001)_{\epsilon} || [1-10]_{\gamma} || [1-210]_{\epsilon}$  orientation relationship and (b) in the 28%Mn alloy, mechanical twinning in two variants (edge on). SAD patterns (insets) were recorded from [110] zones while the BF images were recorded slightly off axis in nominally two beam conditions.

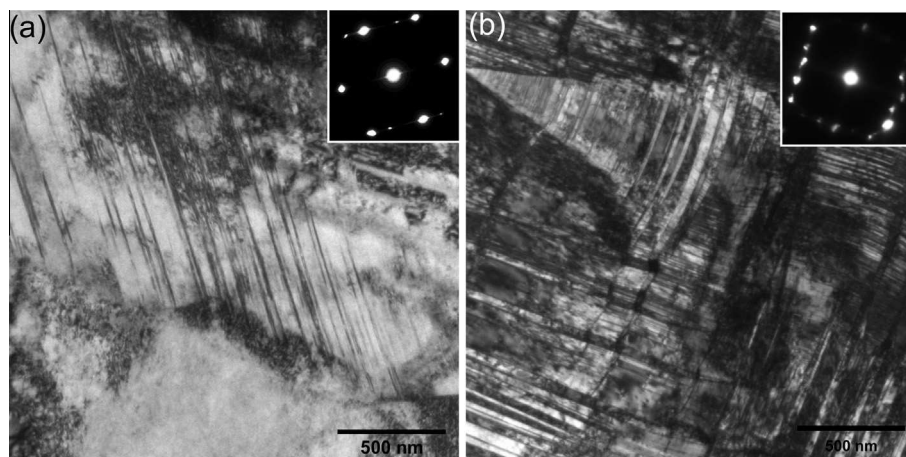


**Fig. 8.** TEM BF micrographs of mechanical twinning after 0.34 true strain in (a) the 22%Mn alloy and (b) two variants in the 28%Mn alloy. SAD patterns (insets) were recorded from [110] zones while the BF images were recorded off axis in nominally two beam conditions.

in the surface temperature of the sample due to adiabatic heating during tensile testing is  $\sim 5$  °C in the region of necking just prior to failure, as measured by a thermal camera during a test of the 28%

Mn alloy (Fig. 10). This 5 °C temperature rise corresponds to a negligible SFE increase of less than  $1 \text{ mJ m}^{-2}$  according to thermodynamic calculations [18].

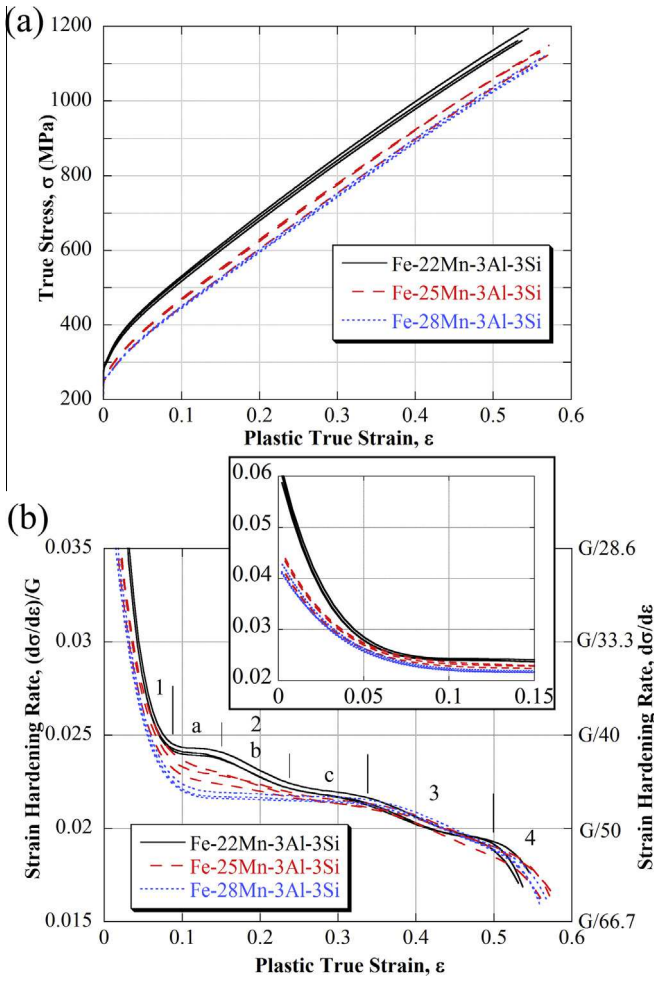


**Fig. 9.** (a) True stress and (b) strain-hardening rate vs. plastic true strain for the Fe-22/25/28Mn-3Al-3Si steels (3 tests for each composition). The strain-hardening stages are labeled 1–4 at their approximate locations and all curves terminate at maximum uniform elongation. The inset shows the hardening rates at low strains.

The mechanical properties are summarized in Table 3. The yield strength of the 22%Mn alloy is  $\sim 13\%$  larger than that of the 25 and 28%Mn alloys. Small reductions in ultimate tensile strength (UTS), true ultimate tensile strength (TUTS) and toughness (calculated by integrating the engineering stress strain curve) occur with increasing SFE from 15 to 39  $\text{mJ m}^{-2}$ . The largest uniform ( $\phi_{\text{unf}}$ ), post-uniform ( $\phi_{\text{p-unf}}$ ) and total ( $\phi_{\text{total}}$ ) elongation occur in the 25%Mn alloy with a SFE of 21  $\text{mJ m}^{-2}$ . Only the yield strengths and post uniform elongations differ by  $>10\%$  among the three alloys, despite a large difference in the SFEs and deformation mechanisms.

## 5. Discussion

### 5.1. Influence of SFE on yield strength

Previous authors showed that the yield stress ( $\sigma_{\text{YS}}$ ) of austenitic FeMnC(Al) TWIP steels [28,32], austenitic stainless steels [47,48] and other fcc materials such as Cu [49] exhibit two temperature regimes: (1) a higher temperature “athermal” regime where  $\sigma_{\text{YS}}$  exhibits only weak temperature sensitivity and (2) a lower temperature “thermal” regime of thermally activated dislocation motion where  $\sigma_{\text{YS}}$  exhibits relatively strong temperature sensitivity. Consequently,  $\sigma_{\text{YS}}$  may be approximated from the athermal ( $\sigma_{\text{Athermal}}$ ) and thermal ( $\sigma_{\text{Thermal}}$ ) contributions using a superposition law as shown in Eq. (1) [28,32].

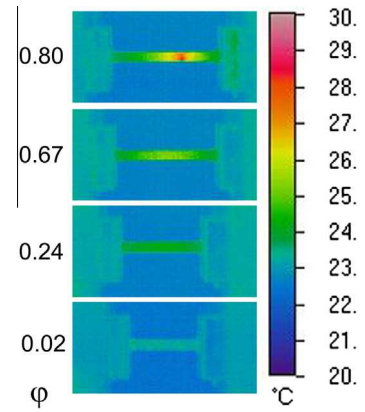


**Fig. 10.** Thermal images obtained by a calibrated infrared camera of the 28%Mn alloy during tensile testing at different intervals of plastic strain ( $\phi$ ).

**Table 3**

Summary of the yield strength, ultimate tensile strength (UTS), true ultimate tensile strength (TUTS) and toughness, along with uniform ( $\phi_{\text{unf}}$ ), post-uniform ( $\phi_{\text{p-unf}}$ ) and total elongation ( $\phi_{\text{total}}$ ) of the 22, 25 and 28%Mn alloys. The sum of  $\phi_{\text{unf}}$  and  $\phi_{\text{p-unf}}$  may differ slightly from  $\phi_{\text{total}}$  due to rounding. The uncertainty represents the standard deviation from 3 tests.

Parameter	22%Mn	25%Mn	28%Mn	% Maximum difference of values
Yield strength (MPa)	$293 \pm 3$	$264 \pm 5$	$259 \pm 2$	13
UTS (MPa)	$684 \pm 7$	$642 \pm 7$	$631 \pm 5$	8
TUTS (MPa)	$1172 \pm 19$	$1136 \pm 9$	$1106 \pm 14$	6
$\phi_{\text{unf}}$ (%)	$73.0 \pm 1.7$	$76.9 \pm 1.9$	$76.1 \pm 1.2$	5
$\phi_{\text{p-unf}}$ (%)	$12.2 \pm 1.0$	$13.8 \pm 0.7$	$10.7 \pm 1.1$	29
$\phi_{\text{total}}$ (%)	$85.1 \pm 2.6$	$90.6 \pm 1.5$	$86.8 \pm 2.2$	6
Toughness ( $\text{mJ mm}^{-3}$ )	$513 \pm 23$	$506 \pm 9$	$470 \pm 16$	9

$$\sigma_{\text{YS}} = \sigma_{\text{Athermal}} + \sigma_{\text{Thermal}} \quad (1)$$

$\sigma_{\text{Athermal}}$  contributes at all temperatures and is primarily comprised of solid solution ( $\sigma_{\text{SS}}$ ) and Hall–Petch strengthening ( $\sigma_{\text{H-P}}$ ) [28,32]. The quantities  $\sigma_{\text{SS}}$ ,  $\sigma_{\text{H-P}}$ , and consequently,  $\sigma_{\text{Athermal}}$ , scale approximately with the elastic modulus [28,32] and exhibit a small, approximately linear, dependence on temperature [4,32]. For FeMnC steels, the linear dependence on temperature of  $\sigma_{\text{Athermal}}$  was reported to be approximately  $-0.25 \text{ MPa } ^{\circ}\text{C}^{-1}$  by analysis of yield strength data obtained at temperatures above RT where the contribution of  $\sigma_{\text{Thermal}}$  is negligible [32]. A much steeper increase in the yield strength with decreasing temperature occurs below RT in FeMnC steels [4,32] and corresponds to the onset of  $\sigma_{\text{Thermal}}$  and the thermally activated range of dislocation motion.  $\sigma_{\text{Thermal}}$  continually increases with decreasing temperature as less thermal energy is available to assist dislocations in overcoming short-range obstacles [49].  $\sigma_{\text{Thermal}}$  is also sensitive to certain alloying additions, increasing with increasing C (up to  $\sim 0.6 \text{ wt.}\%$ ) [32], N [47,48] and Si [32] content. However,  $\sigma_{\text{Thermal}}$  is reported to be insensitive to Mn and Al additions as well as magnetic state [4,32].

In the present work, the RT yield strength of the 22%Mn alloy is  $293 \pm 3 \text{ MPa}$  and is  $\sim 12\%$  greater than the yield strengths of the 25 and 28%Mn alloys,  $264 \pm 5$  and  $259 \pm 2 \text{ MPa}$ , respectively, as summarized in Table 3. The grain size of each alloy is approximately 21  $\mu\text{m}$  and additions of Mn from 25 to 28 wt.% result in a decrease in yield strength of  $\sim 2 \text{ MPa}$  per wt.%, agreeing well with a small decrease of 1.6 MPa per wt.% addition of Mn for Fe-xMn-2Al-0.7C ( $x = 16, 18$  and 20 wt.%) alloys reported by De Cooman et al. [6]. Therefore, neither grain size differences nor solid solution strengthening due to Mn reduction can entirely explain the significantly greater yield stress of the 22%Mn alloy. Fig. 11 shows the



yield strengths of the three alloys as a function of temperature from RT to 400 °C (the elevated temperature data is obtained from [43]). A steep increase in the yield strength of each alloy occurs with decreasing temperature below approximately 200 °C, corresponding to the onset of the thermally activated range of dislocation glide. In particular, a much larger increase in the yield stress from 100 °C to RT is observed in the 22%Mn alloy. The onset temperature ( $\sim 200$  °C) of the thermally activated range of dislocation glide in the present alloys is substantially greater than  $\sim$ RT for FeMnC alloys and the higher transition temperature is likely due to additions of Si as previously reported [32]. At 200 °C and above, the yield strength is assumed to be entirely comprised of  $\sigma_{\text{Athermal}}$ . Linear fits of the yield strengths at 200, 300 and 400 °C for each alloy, and extrapolated to RT, approximate the magnitude and small temperature dependence of  $\sigma_{\text{Athermal}}$  and are shown in Fig. 11. The larger athermal contribution to the yield stress of the 22%Mn alloy is primarily attributed to greater solid solution strengthening from Mn reduction and the small amount of ferrite present ( $<1\%$ ) in the microstructure since no significant variations in grain size were observed between the three alloys.

The values of  $\sigma_{\text{Thermal}}$  at 100 °C for the 22, 25 and 28%Mn alloys are similar at 29, 25 and 29 MPa, respectively. The small variations in the values may relate to uncertainties in the data and no significant influence of Mn on  $\sigma_{\text{Thermal}}$  is observed, consistent with previous reports on the influence of Mn [32]. However,  $\sigma_{\text{Thermal}}$  at RT is calculated to be approximately 100, 82 and 74 MPa, respectively. The increase in  $\sigma_{\text{Thermal}}$  from 100 °C to RT is substantially greater in the 22%Mn alloy than for the 25 and 28%Mn alloys. The RT value of  $\sigma_{\text{Thermal}}$  in the 22%Mn steel is 18 and 26 MPa greater, respectively, than the corresponding values for the 25 and 28%Mn alloys. The findings suggest that reducing the SFE below a value of approximately  $21 \text{ mJ m}^{-2}$ , either by reducing the alloy temperature or by reducing Mn content, results in a large increase in  $\sigma_{\text{Thermal}}$ . The increase is likely attributed to differences in the characteristics of dislocation glide among the three alloys at RT. Microstructural observations of the 22%Mn alloy after RT deformation to 0.03 true strain show minimal cross slip and dislocations exhibit large dissociation widths (e.g., Fig. 3a and b) compared to the 25% (Fig. 3c) and especially, the 28%Mn alloy (Fig. 3d). Dislocation cross slip, a thermally activated and stress assisted process [49], is made more difficult by the low SFE ( $15 \text{ mJ m}^{-2}$ ). Therefore, cross slip of dislocations to planes more favorably oriented for slip, or to overcome obstacles, will require additional normal stress in the 22%Mn alloy. The larger thermal component also contributes significantly to the greater flow stress observed in the 22%Mn alloy, relative to the 25% and 28%Mn alloys, over the entire range of deformation.

## 5.2. Microstructural influence on strain-hardening – 0 to 0.1 true strain

Stage 1 strain-hardening is characterized by a sharp decrease in the strain-hardening rate for each alloy similar to classical stage III hardening [46]. This stage depends strongly on material, SFE, temperature and strain rate and is typically associated with dynamic recovery processes including cross-slip, annihilation of screw dislocations of opposite signs and the formation of low-energy dislocation structures (LEDs) like tangles and cells [50–52]. Dynamic recovery lowers the average strain energy of the dislocation structure making it easier to generate new dislocations to further strain the material [51]. These processes are inhibited by lowering the SFE, which, along with the friction stress, plays a major role in the ability of two partial dislocations to re-combine and cross slip onto a more favorable slip plane [39,46,51,53]. The friction stress is predominately a function of  $G$ , the atomic misfit parameter and the

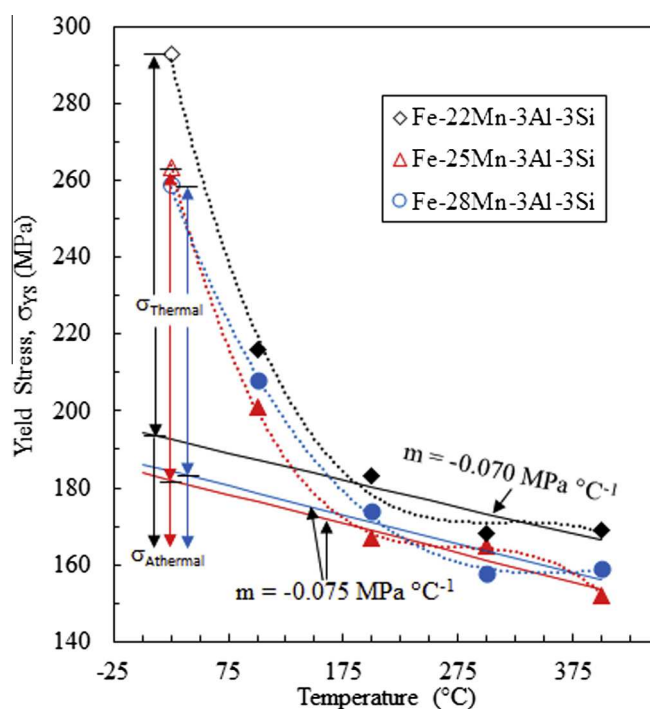


Fig. 11. Yield strength vs. temperature for the Fe-22/25/28Mn-3Al-3Si steels. The RT yield strength is the average from 3 tensile tests. The yield strengths corresponding to 100, 200, 300 and 400 °C (filled data points) are taken from [43]. The straight lines are linear fits to the yield strengths of each alloy at 200, 300 and 400 °C and approximate the athermal contribution to the yield strength. The slopes ( $m$ ) of the linear fits are indicated. The approximate magnitudes of the athermal and thermal contributions to the yield strength at RT are denoted.

solute content [39] and is similar in the present materials, suggesting the propensity for cross slip is primarily controlled by the SFE.

The 22%Mn alloy has the lowest SFE ( $15 \text{ mJ m}^{-2}$ ) of the three materials and the highest strain-hardening rate in this stage, particularly from 0 to 0.03 true strain (see Fig. 9b). The low SFE of this alloy strongly impedes cross slip and confines dislocations to single slip planes, thereby limiting their mobility, as evidenced by Fig. 3a and b. Large stacking faults and  $\epsilon_{\text{hcp}}$ -martensite lath structures form at the onset of yielding [18] in the 22%Mn alloy and serve as impediments to dislocations gliding on non-coplanar slip planes (Fig. 3b), further reducing dislocation mobility and dynamic recovery. Dislocation pile ups at the  $\epsilon_{\text{hcp}}$ -martensite lath/matrix interface will result in a back stress contribution to the flow stress which depends, among other factors, inversely on the mean spacing between laths [14]. This back stress contribution to the flow stress and work-hardening at low strains will be greater than that for the two higher-SFE alloys where cross slip is easier and mechanical twinning, which requires a critical stress and dislocation density [16], is not yet a significant strengthening mechanism. Furthermore, the thermal and athermal components to the flow stress also are also greater in the 22%Mn alloy (discussed in Section 5.1).

The 25%Mn alloy has a SFE of  $21 \text{ mJ m}^{-2}$  and the deformation microstructure after 0.03 true strain exhibits both planar and wavy characteristics, as evidenced by stacking faults and curved or wavy dislocations in Fig. 3c. Wavy dislocations are typically associated with greater mobility and ease of cross slip [54] suggesting the beginning of the transition from planar to wavy slip coincides with an increase in SFE from 15 to  $21 \text{ mJ m}^{-2}$ . The greater dislocation mobility at low strains is due to increased ability for cross slip and fewer strain-induced planar obstacles, resulting in a lower hardening rate than is observed in the 22%Mn alloy.

The SFE of the 28%Mn alloy is  $39 \text{ mJ m}^{-2}$  and the microstructure at 0.03 true strain is more typical of a medium SFE alloy, with wavy dislocations that are predominately constricted like those in Fig. 3d. The dislocation structure, which includes a significant portion of fine tangles, indicates that cross slip is more favorable and dislocation mobility is greater in this alloy due to a higher SFE. The dislocation density is shown to be a key parameter to describe the strain hardening in fcc materials [46] and high Mn TWIP steels [4,6,11,14,16,28,45,55]. Enhanced dynamic recovery and the absence of mechanical twins to trap dislocations at this strain in the 28%Mn alloy will lower the average dislocation density relative to the 22% and 25%Mn alloys. As such, the flow stress and strain-hardening rates at low strains in the 28%Mn alloy are slightly lower than in the 25%Mn alloy and substantially lower than in the 22%Mn alloy. The strain-hardening rate in stage 1 for these materials exhibits a significant sensitivity to the SFE when the SFE is in the range from 15 to  $21 \text{ mJ m}^{-2}$  but is less sensitive to changes in the SFE from 21 to  $39 \text{ mJ m}^{-2}$ .

### 5.3. Microstructural influence on strain-hardening – 0.1 to 0.34 true strain

The transition from stage 1 to 2 hardening can occur when the rate of dynamic recovery of dislocations stabilizes [46,56,57]. The occurrence of the transition from stage 1 to 2 at a higher strain hardening rate in the 22%Mn alloy indicates a smaller rate of dynamic recovery in this alloy at this level of strain. At 0.1 true strain in the 22%Mn alloy,  $\epsilon_{\text{hcp}}$ -martensite laths were identified by SAD in 45% of observed grains (see Table 2), exhibiting significantly higher activity than mechanical twinning in the 25 and 28%Mn alloys at the same strain. The formation of  $\epsilon_{\text{hcp}}$ -martensite rather than mechanical twinning is consistent with a negative value of  $\Delta G^{\text{fcc} \rightarrow \text{hcp}} = -88 \text{ J mol}^{-1}$  (see Table 1). Structures with multiple variants of  $\epsilon_{\text{hcp}}$ -martensite laths were observed, such as shown in Fig. 4b, whereas mechanical twinning in the 25 and 28%Mn alloys was limited to only a single variant within any given grain after the same strain. These factors contribute to the enhanced strain-hardening in stages 2a and b of the 22%Mn alloy compared to the other alloys, despite the small volume fractions of  $\epsilon_{\text{hcp}}$ -martensite measured by XRD in the 22%Mn alloy (see Fig. 1). It should be noted that XRD may slightly underestimate the amount of  $\epsilon_{\text{hcp}}$ -martensite present in the microstructure of the 22%Mn alloy due to the small apparent thickness of the laths, particularly at low strains. The role of  $\epsilon_{\text{hcp}}$ -martensite on the RT strain-hardening behavior is further elucidated from elevated temperature tensile testing (100–400 °C) [43], where  $\epsilon_{\text{hcp}}$ -martensite is predominately suppressed and stages 2a and b are absent and replaced by a single region of uniform and reduced strain-hardening. The beginning of stage 2b is characterized by a 2nd inflection in the strain-hardening rate at  $\sim 0.15$  true strain which leads to a decrease in the hardening rate up to 0.25 true strain. Interestingly, this decrease in hardening rate precedes the maximum rate of  $\epsilon_{\text{hcp}}$ -martensite formation at  $\sim 0.25$  true strain (see Fig. 1). One possible explanation for this behavior is that increases in the volume of  $\epsilon_{\text{hcp}}$ -martensite occur by preferentially thickening existing laths, leading to larger, more energetically favorable regions of ABAB stacking while decreasing the rate of mean free path reduction and strain hardening. Qualitative observations in the present work and by other authors [40,41] suggest the apparent thickness of  $\epsilon_{\text{hcp}}$ -martensite laths increases with strain. The onset of stage 2c occurs with a third inflection in the strain-hardening rate at  $\sim 0.25$  true strain, approximately coinciding with maximum rates of  $\alpha_{\text{bcc}}$ -martensite formation (see Fig. 1). Grässel et al. [1] and Tomota et al. [58] observed similar inflections in the strain-hardening rate that corresponded to high rates of

$\alpha_{\text{bcc}}$ -martensite transformation in Fe–15/20Mn–3Al–3Si and binary Fe–Mn alloys, respectively.

Observations of the microstructure of the 25%Mn alloy after 0.1 and 0.18 true strain revealed both  $\epsilon_{\text{hcp}}$ -martensite lath structures and mechanical twinning. Dislocation accumulation occurred at the twin and  $\epsilon$ -martensite interfaces with the austenite matrix, particularly at 0.18 true strain, indicating their effectiveness as obstacles to dislocation glide. The activation of both mechanical twinning and  $\epsilon_{\text{hcp}}$ -martensite formation is related to the SFE of  $21 \text{ mJ m}^{-2}$  and the value of  $\Delta G^{\text{fcc} \rightarrow \text{hcp}} = 31 \text{ J mol}^{-1}$ , which is sufficiently close to zero that mechanical twinning and  $\epsilon_{\text{hcp}}$ -martensite formation are both possible during deformation [12]. The ratio of grains with mechanical twins vs. grains with  $\epsilon_{\text{hcp}}$ -martensite is  $\sim 2:1$  (see Table 2), reflecting the positive value of  $\Delta G^{\text{fcc} \rightarrow \text{hcp}}$ , and did not change significantly from 0.1 to 0.18 true strain. Less  $\epsilon_{\text{hcp}}$ -martensite forms in the 25%Mn alloy than in the 22%Mn alloy, resulting in lower strain-hardening rates in the 25%Mn alloy up to  $\sim 0.25$  true strain. Furthermore, the higher SFE delayed the onset of secondary deformation mechanism formation in more than one slip system to  $\sim 0.18$  true strain (see Fig. 2b), also contributing to the lower strain-hardening rate relative to the 22%Mn alloy.

At 0.1 true strain  $\sim 25\%$  of grains contain primary mechanical twins in the 28%Mn alloy. These mechanical twins serve as barriers to dislocation glide on non-coplanar slip systems but have only a minimal impact on slip occurring in coplanar systems [44]. The strain-hardening rates of the 28%Mn alloy are nearly identical at RT and elevated temperatures (200–400 °C) from 0 to 0.1 true strain [43], even though no mechanical twinning occurs in this strain interval at elevated temperature. The finding suggests that mechanical twinning has no significant influence on the mechanical properties from 0 to 0.1 true strain and is not directly related to the interruption of stage 1, consistent with results of Gutiérrez-Urrutia and Raabe [9], who found that the transition from stage 1 to 2 strain-hardening of an Fe–22Mn–0.6C TWIP steel was caused by evolution of the dislocation substructure rather than mechanical twinning. These observations are in contrast to those of Asgari et al. [50], who specifically attributed the interruption of stage 1 and the onset of stage 2 in low SFE MP35N and 70/30 brass to primary mechanical twinning during compression testing. However, from  $\sim 0.12$  to 0.34 true strain the 28%Mn alloy exhibits a nearly constant strain-hardening rate of 0.022, which is attributed to grain refinement and reduction of the mean free path of dislocation glide by both dislocation substructure evolution and mechanical twinning (see Figs. 6a and b, 7b and 8b). At elevated temperatures from 200 to 400 °C, a significant decrease in strain-hardening rates from 0.12 true strain to failure occurs in the absence of mechanical twinning, illustrating the strong influence that mechanical twinning has on the RT strain-hardening [43]. The onset of the formation of multiple variants of mechanical twins within a single grain (Fig. 7b) at RT between 0.1 and 0.18 true strain provides additional strain-hardening by trapping dislocations at the twin boundaries, as is evident in Figs. 7b after 0.18 true strain and 8b after 0.34 true strain.

### 5.4. Microstructural influence on strain-hardening – 0.34 true strain to failure

Each alloy experiences an inflection in the strain-hardening rate near 0.34 true strain, followed by a gradual decrease in the strain-hardening rate until stage 4. The significantly higher work-hardening rates in stage 3 at RT compared to elevated temperatures (200–400 °C) [43], where secondary deformation mechanisms are largely suppressed, indicate that  $\epsilon_{\text{hcp}}$ -martensite and mechanical twins continue to enhance the strain-hardening albeit to a

lesser extent than in stage 2. XRD analysis indicates a decrease in the rate of martensite formation during stage 3 in the 22%Mn alloy (see Fig. 1). In contrast, microstructural observations by optical microscopy qualitatively indicate that a significant increase in mechanical twin fraction occurs from 0.34 true strain until maximum uniform elongation in the 25 (see Fig. 2c and d) and 28% Mn alloys. This result is consistent with those of other authors who report a decreasing strain-hardening rate despite a significant increase in the mechanical twin fraction during the final stages of deformation in the Fe–22Mn–0.6C TWIP steel [2,9], attributed to the reduced capability of the microstructure to trap more dislocations [9]. The nearly identical strain-hardening rates of the three alloys in stage 3 indicate that differences in the SFE between 15 and 39  $\text{mJ m}^{-2}$  and the type of secondary deformation mechanisms have a limited influence on the work hardening behavior during stage 3 hardening.

The sharp decrease in work-hardening rate characteristic of stage 4 is more abrupt and severe in the 22%Mn alloy and maximum uniform elongation occurs earlier than in the 25 and 28% Mn alloys. These factors indicate the capacity of the microstructure to further harden in the 22%Mn alloy is reached prior to that of the 25 and 28%Mn alloys, likely due to the greater amount hardening that occurred in the 22%Mn alloy at earlier strains.

### 5.5. Influence of SFE on tensile strength and ductility

The small decrease in UTS that occurs with increasing SFE is attributed to changes in the deformation mechanisms. The contribution to the flow stress from thermally activated dislocation motion, discussed in Section 5.1, decreases significantly with increasing SFE from 15 to 21  $\text{mJ m}^{-2}$  and more gradually from 21 to 39  $\text{mJ m}^{-2}$ . In addition, the formation of  $\alpha/\varepsilon$ -martensite earlier in the deformation sequence compared to mechanical twinning enhances the strain-hardening and UTS at the expense of total elongation in the 22%Mn alloy. Conversely, the nucleation of mechanical twins requires a critical stress and dislocation density, delaying their onset and corresponding hardening contribution until later stages of deformation [16], which reduces UTS. Furthermore, the reorientation of the austenite matrix by mechanical twinning or “texture softening”, may also generate new more favorable orientations for slip [59], and reduce the hardening contribution of mechanical twinning relative to  $\varepsilon$ -martensite formation.

The 25%Mn alloy with a SFE of 21  $\text{mJ m}^{-2}$  exhibits only marginally better uniform elongation than 28%Mn alloy but a more substantial increase in uniform elongation relative to the 22%Mn alloy. The optimal SFE for maximum uniform elongation is dependent on multiple factors. If the SFE is too low,  $\varepsilon$ - and/or  $\alpha$ -martensite are the dominant secondary deformation mechanisms and hardening is concentrated in the early and intermediate stages of deformation [1,16], leading to premature exhaustion of the hardening as evidenced by the abrupt decrease in strain-hardening rate in stage 4 and lower uniform elongations in the 22%Mn alloy. Conversely, a SFE that is too high will delay the onset and reduce the intensity of mechanical twinning, resulting in lower ductility and strength [16]. The trend in post uniform elongation among the three alloys is similar. The post uniform elongation in the 25%Mn alloy is substantially greater than that of the 28%Mn alloy and moderately better than that of the 22%Mn alloy (Table 3). Post uniform elongation is typically influenced by strain rate sensitivity (particularly for Fe–Mn–C TWIP steels [6]) and damage evolution. Grässel et al. [1] reported no significant strain rate sensitivity of the UTS from strain rates of  $10^{-4}$  to  $10^{-3} \text{ s}^{-1}$  in both Fe–20Mn–3Al–3Si and Fe–25Mn–3Al–3Si alloys and only a small positive strain rate sensitivity of the yield stress in the Fe–20Mn–3Al–3Si alloy. An apparent increase in positive strain rate

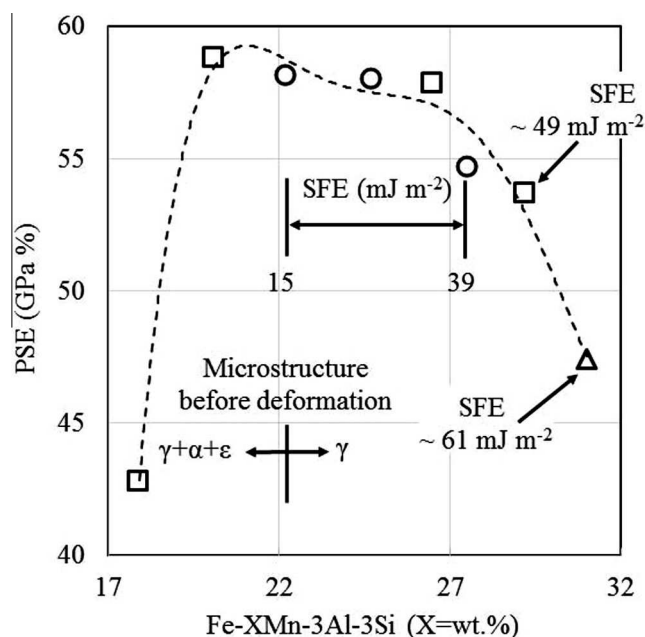


Fig. 12. PSE for Fe–XMn–3Al–3Si alloys (circles present, squares [1,19] and triangle [61]). The SFEs of 49 and 61  $\text{mJ m}^{-2}$  are extrapolated from relationships proposed by Pierce et al. [18].

sensitivity of the yield stress with decreasing Mn content in Fe–xMn–3Al–3Si wt.% steels reported by Grässel et al. [1] is insufficient to explain the large increase in post uniform elongation of the 25%Mn alloy relative to the 22 and 28%Mn alloys in the present work. Gutiérrez-Urrutia and Raabe [60] noted that damage mechanisms triggered by local stress concentrations at grain boundaries may be accentuated in microstructures containing dense planar dislocation structures. Therefore, stress concentrations at grain boundaries might be minimized in the 28%Mn alloy where cross slip is easiest and the microstructures exhibit less planarity yet this alloy exhibits the lowest post uniform elongation. Alternatively, the larger post uniform elongation in the 25%Mn alloy is likely due to a SFE value that results in optimal work hardening during necking, similar to the cause of the enhanced uniform elongation in the 25%Mn alloy. The slopes of the strain hardening rates at max uniform elongation are significantly steeper for the 22 and 28%Mn alloys (Fig. 9b), suggesting the work hardening capacity in the post uniform elongation region will be less in these alloys. Therefore, differences in the post uniform elongation among the three alloys are primarily attributed to differences in SFE. Interestingly, the post uniform elongation appears to be significantly more sensitive to SFE value, based on the percentage change among the three alloys, than the uniform elongation (see Table 3). Similarly, Mosecker et al. [48] reported that the post uniform elongation as a function of temperature in an Fe–14Cr–16Mn–0.3C–0.3N wt.% steel alloy exhibited a pronounced peak near RT (also at a SFE of 21  $\text{mJ m}^{-2}$ ).

The product of ultimate tensile strength and total elongation (PSE) as a function of Mn content for Fe–xMn–3Al–3Si alloys from the present work and literature [1,19,61] is shown in Fig. 12. The estimated SFEs of the Fe–29/31Mn–3Al–3Si alloys [1,19,61] are 49 and 61  $\text{mJ m}^{-2}$ , respectively. The SFE range from 15 to 39  $\text{mJ m}^{-2}$  results in excellent strength and ductility and can serve as guidelines for the design of high-Mn austenitic steel. The substantial decrease in PSE for SFEs above 39  $\text{mJ m}^{-2}$  is associated with a progressive reduction and/or delay of mechanical twinning [16]. These observations are consistent with those of Saeed-Akbari et al. [7,8], who observed excellent strength and ductility in TWIP



steels with calculated SFEs of  $19\text{--}35\text{ mJ m}^{-2}$  but substantially reduced mechanical properties in an alloy with SFE of  $50\text{ mJ m}^{-2}$ .

## 6. Summary and conclusions

The present study investigated the influence of SFE on the microstructural and strain-hardening evolution of three (Fe–22/25/28Mn–3Al–3Si) transformation- and twinning-induced plasticity (TRIP/TWIP) steels during RT tensile deformation. The RT stacking fault energies of the Fe–22/25/28Mn–3Al–3Si alloys increase from 15, to 21, to  $39\text{ mJ m}^{-2}$ , as the Mn content systematically increases. The small solid solution strengthening of Mn, use of experimentally measured SFEs and experimental conditions to limit adiabatic heating during plastic deformation (quasi-static strain rates and sub-sized tensile specimens) allowed the influence of SFE on mechanical properties to be directly ascertained. The following important conclusions were drawn from this work:

- The range of SFE from  $15\text{ to }39\text{ mJ m}^{-2}$  results in an excellent combination of UTS and total elongation ( $55\text{--}58\text{ GPa\%}$ ) with only small variations in strength and ductility, despite the transitioning of the steels from TRIP- to TWIP-dominated behavior, and can serve as guidelines for the design of high-Mn austenitic steels. Comparisons with data from the literature indicate the strength and ductility decrease significantly above a SFE of approximately  $39\text{ mJ m}^{-2}$ , corresponding to a reduction in mechanical twinning.
- A SFE of  $15\text{ mJ m}^{-2}$  (Fe–22Mn–3Al–3Si) resulted in a deformation microstructure dominated by highly planar slip, suppression of dislocation cross-slip, enhanced yield strength, and  $\alpha_{\text{bcc}}/\epsilon_{\text{hcp}}$ -martensite transformation as the dominant secondary deformation mechanisms. The onset of grain refinement due to the formation of multiple variants of  $\epsilon_{\text{hcp}}$ -martensite within any given grain occurs from the beginning of plastic deformation and provides superior work-hardening at low and intermediate strains ( $0\text{--}0.34$  true strain), higher strength, and lower elongation.
- A SFE of  $21\text{ mJ m}^{-2}$  (Fe–25Mn–3Al–3Si) resulted in a dislocation structure that exhibits both planar and wavy characteristics. The formation of  $\epsilon_{\text{hcp}}$ -martensite and mechanical twinning results in excellent strain-hardening in the initial, intermediate and final stages of deformation, along with the largest elongation of the three alloys.
- At low strains ( $0\text{ to }0.1$  true strain), a SFE of  $39\text{ mJ m}^{-2}$  (Fe–28Mn–3Al–3Si) facilitates greater dislocation cross slip and mobility which reduces work-hardening in comparison to the lower SFE alloys. The formation of  $\epsilon_{\text{hcp}}$ -martensite is predominantly suppressed over the entire range of deformation. Mechanically twinning is not activated from  $0\text{ to }0.03$  true strain and provides no substantial contribution to hardening from  $0\text{ to }0.1$  true strain. From  $\sim 0.1$  true strain to failure, mechanical twinning significantly enhances the strain-hardening, resulting in excellent ductility but the lowest strength of the three alloys.

## Acknowledgements

This work is sponsored by the National Science Foundation Division of Materials Research, USA, under Grant DMR0805295 and by the Ministry of Science and Innovation of Spain, under Grant MAT2012-39124. DTP gratefully acknowledges support for extended visits to CSIC, Madrid and MPI, Düsseldorf during his time as a graduate student at Vanderbilt University where most of this research was performed. The authors are thankful for insightful comments provided by an anonymous reviewer.

## References

- [1] O. Grässel, L. Krüger, G. Frommeyer, L.W. Meyer, High strength Fe–Mn–(Al, Si) TRIP/TWIP steels development – properties – application, *Int. J. Plasticity* 16 (2000) 1391–1409.
- [2] D. Barbier, N. Gey, S. Allain, N. Bozzolo, M. Humbert, Analysis of the tensile behavior of a TWIP steel based on the texture and microstructure evolutions, *Mater. Sci. Eng. A* 500 (2009) 196–206.
- [3] S. Curtze, V.T. Kuokkala, Dependence of tensile deformation behavior of TWIP steels on stacking fault energy, temperature and strain rate, *Acta Mater.* 58 (2010) 5129–5141.
- [4] O. Bouaziz, S. Allain, C.P. Scott, P. Cugy, D. Barbier, High manganese austenitic twinning induced plasticity steels: a review of the microstructure properties relationships, *Curr. Opin. Solid State Mater. Sci.* 15 (2011) 141–168.
- [5] S. Vercammen, Processing and tensile behaviour of TWIP steels microstructural and textural analysis (Ph.D. thesis), Leuven, University of Leuven, 2004.
- [6] B.C. De Cooman, O. Kwon, K.-G. Chin, State of the knowledge on TWIP steel, *J. Mater. Sci. Technol.* 28 (2012) 513–527.
- [7] A. Saeed-Akbari, L. Mosecker, A. Schwedt, W. Bleck, Characterization and prediction of flow behavior in high-manganese twinning induced plasticity steels: Part 1. Mechanism maps and work-hardening behavior, *Metall. Mater. Trans. A* 43 (2012) 1688–1704.
- [8] A. Saeed-Akbari, A. Schwedt, W. Bleck, Low stacking fault energy steels in the context of manganese-rich iron-based alloys, *Scr. Mater.* 66 (2012) 1024–1029.
- [9] I. Gutiérrez-Urrutia, D. Raabe, Dislocation and twin substructure evolution during strain hardening of an Fe–22 wt.% Mn–0.6 wt.% C TWIP steel observed by electron channeling contrast imaging, *Acta Mater.* 59 (2011) 6449–6462.
- [10] J. Kim, S.-J. Lee, B.C. De Cooman, Effect of Al on the stacking fault energy of Fe–18Mn–0.6C twinning-induced plasticity, *Scr. Mater.* 65 (2011) 363–366.
- [11] K. Jeong, J.-E. Jin, Y.-S. Jung, S. Kang, Y.-K. Lee, The effects of Si on the mechanical twinning and strain hardening of Fe–18Mn–0.6C twinning-induced plasticity steel, *Acta Mater.* 61 (2013) 3399–3410.
- [12] L. Mosecker, A. Saeed-Akbari, Nitrogen in chromium-manganese stainless steels: a review on the evaluation of stacking fault energy by computational thermodynamics, *Sci. Technol. Adv. Mater.* 14 (2013) 1–14.
- [13] I. Gutiérrez-Urrutia, D. Raabe, Multistage strain hardening through dislocation substructure and twinning in a high strength and ductile weight-reduced Fe–Mn–Al–C steel, *Acta Mater.* 60 (2012) 5791–5802.
- [14] O. Bouaziz, S. Allain, C. Scott, Effect of grain and twin boundaries on the hardening mechanisms of twinning-induced plasticity steels, *Scr. Mater.* 58 (2008) 484–487.
- [15] B. Qin, H.K.D.H. Bhadeshia, Plastic strain due to twinning in austenitic TWIP steels, *Mater. Sci. Technol.* 24 (2008) 969–973.
- [16] D.R. Steinmetz, T. Jäpel, B. Wietbrock, P. Eisenlohr, I. Gutiérrez-Urrutia, A. Saeed-Akbari, T. Hickel, F. Roters, D. Raabe, Revealing the strain-hardening behavior of twinning-induced plasticity steels: theory, simulations, experiments, *Acta Mater.* 61 (2013) 494–510.
- [17] I. Gutiérrez-Urrutia, S. Zaefferer, D. Raabe, The effect of grain size and grain orientation on deformation twinning in a Fe–22 wt.% Mn–0.6 wt.% C TWIP steel, *Mater. Sci. Eng. A* 527 (2010) 3552–3560.
- [18] D.T. Pierce, J.A. Jiménez, J. Bentley, D. Raabe, C. Oskay, J.E. Wittig, The influence of manganese content on the stacking-fault and austenite/ $\epsilon$ -martensite interfacial energies in Fe–Mn–(Al–Si) steels investigated by experiment and theory, *Acta Mater.* 68 (2014) 238–253.
- [19] O. Grässel, G. Frommeyer, C. Derder, H. Hofmann, Phase transformations and mechanical properties of Fe–Mn–Al–Si TRIP steels, *J. Physique IV France* 7 (1997) 383–386. Colloque C5.
- [20] S. Allain, J.P. Chateau, O. Bouaziz, S. Migot, N. Guelton, Correlations between the calculated stacking fault energy and the plasticity mechanisms in Fe–Mn–C alloys, *Mater. Sci. Eng. A* 387–389 (2004) 158–162.
- [21] A. Dumay, J.-P. Chateau, S. Allain, S. Migot, O. Bouaziz, Influence of addition elements on the stacking-fault energy and mechanical properties of an austenitic Fe–Mn–C steel, *Mater. Sci. Eng. A* 483–484 (2008) 184–187.
- [22] A. Saeed-Akbari, J. Imlau, U. Pahl, W. Bleck, Derivation and variation in composition-dependent stacking fault energy maps based on subregular solution model in high-manganese steels, *Metall. Mater. Trans. A* 40 (2009) 3076–3090.
- [23] J.E. Wittig, M. Pozuelo, J.A. Jiménez, G. Frommeyer, Temperature dependant deformation mechanisms of a high-nitrogen manganese austenitic stainless steel, *Stl. Res. Int.* 80 (2009) 66–70.
- [24] M. Koyama, E. Akiyama, T. Sawaguchi, D. Raabe, K. Tsuzaki, Hydrogen-induced cracking at grain and twin boundaries in and Fe–Mn–C austenitic steel, *Scr. Mater.* 66 (2012) 459–462.
- [25] M. Koyama, E. Akiyama, K. Tsuzaki, D. Raabe, Hydrogen-assisted failure in a twinning-induced plasticity steel studied under in situ hydrogen charging by electron channeling contrast imaging, *Acta Mater.* 61 (2013) 4607–4618.
- [26] M. Koyama, H. Springer, S.V. Merzlikin, K. Tsuzaki, E. Akiyama, D. Raabe, Hydrogen embrittlement associated with strain localization in a precipitation-hardened Fe–Mn–Al–C light weight austenitic steel, *Int. J. Hydrogen Energy* 39 (2014) 4634–4646.
- [27] B.C. De Cooman, K.-G. Chin, J. Kim, High Mn TWIP steels for automotive applications, in: M. Chiaberge (Ed.), *New Trends and Developments in Automotive System Engineering*, InTech, 2011, pp. 101–128.

- [28] I.-C. Jung, B.C. De Cooman, Temperature dependence of the flow stress of Fe–18Mn–0.6C–xAl twinning-induced plasticity steel, *Acta Mater.* 61 (2013) 6724–6735.
- [29] S.-J. Lee, J. Kim, S.N. Kane, B.C. De Cooman, On the origin of dynamic strain aging in twinning-induced plasticity steels, *Acta Mater.* 59 (2011) 6809–6819.
- [30] G.B. Olson, M. Cohen, A general mechanism of martensitic nucleation: Part 1. General concepts and the FCC to HCP transformation, *Metall. Trans. A* 78 (1976) 1897–1904.
- [31] J. Nakano, P.J. Jacques, Effects of the thermodynamic parameters of the hcp phase on the stacking fault energy calculations in the Fe–Mn and Fe–Mn–C systems, *Calphad* 34 (2010) 167–175.
- [32] S. Allain, O. Bouaziz, J.P. Chateau, Thermally activated dislocation dynamics in austenitic FeMnC steels at low homologous temperature, *Scr. Mater.* 62 (2010) 500–503.
- [33] D. Djurovic, B. Hallstedt, J. Von Appen, R. Dronskowski, Thermodynamic assessment of the Fe–Mn–C system, *Calphad* 35 (2011) 479–491.
- [34] S.-J. Lee, Y.-K. Lee, A. Soon, The austenite/e-martensite interface: a first-principles investigation of the fcc Fe(111)/hcp Fe(0001) system, *Appl. Surf. Sci.* 258 (2012) 9977–9981.
- [35] S.M. Cotes, A. Fernandez Guillermet, M. Sade, FCC/HCP martensitic transformation in the Fe–Mn system: part ii. Driving force and thermodynamics of the nucleation process, *Metall. Mater. Trans. A* 35 (2004) 83–91.
- [36] J.E. Wittig, D.T. Pierce, L. Mosecker, A. Saeed-Akbari, M. Beighmohamadi, J. Mayer, TEM investigation of deformation mechanisms in FeMnCrCN TWIP steel, *Microsc. Microanal.* (2013) 1736–1737.
- [37] D.T. Pierce, J. Bentley, J.A. Jiménez, J.E. Wittig, Stacking fault energy measurements of Fe–Mn–Al–Si austenitic twinning-induced plasticity steels, *Scr. Mater.* 66 (2012) 753–756.
- [38] D.T. Pierce, K. Nowag, A. Montagne, J.A. Jiménez, J.E. Wittig, R. Ghisleni, Single crystal elastic constants of high-manganese transformation- and twinning-induced plasticity steels determined by a new method utilizing nanoindentation, *Mater. Sci. Eng. A* 578 (2013) 134–139.
- [39] S.I. Hong, C. Laird, Mechanisms of slip mode modification in f.c.c solid solutions, *Acta Metal. Mater.* 38 (1990) 1581–1594.
- [40] J.W. Brooks, M.H. Loretto, R.E. Smallman, In situ observations of the formation of martensite in stainless steel, *Acta Metall.* 27 (1979) 1829–1838.
- [41] J.W. Brooks, M.H. Loretto, R.E. Smallman, Direct observations of martensite nuclei in stainless steel, *Acta Metall.* 27 (1979) 1839–1847.
- [42] P. Hirsch, A. Howie, R.B. Nicholson, D.W. Pashley, M.J. Whelan, *Electron Microscopy of Thin Crystals*, Robert E. Krieger Publishing Co., Inc, Huntington, NY, 1977.
- [43] D.T. Pierce, The influence of manganese content and temperature on the relative FCC/HCP phase stability and strain-hardening behavior of high-manganese TRIP/TWIP steels (Ph.D. dissertation), Nashville, Vanderbilt University, 2014.
- [44] H. Beladi, I.B. Timokhina, Y. Estrin, J. Kim, B.C. De Cooman, S.K. Kim, Orientation dependence of twinning and strain hardening behaviour of a high manganese twinning induced plasticity steel with polycrystalline structure, *Acta Mater.* 59 (2011) 7787–7799.
- [45] S.R. Kalidindi, Modeling the strain hardening response of low SFE FCC alloys, *Int. J. Plast.* 14 (1998) 1265–1277.
- [46] U.F. Kocks, H. Mecking, Physics and phenomenology of strain hardening: the FCC case, *Prog. Mater. Sci.* 48 (2003) 171–273.
- [47] M.L.G. Byrnes, M. Grujicic, W.S. Owen, Nitrogen strengthening of a stable austenitic stainless steel, *Acta Mater.* 35 (1987) 1853–1862.
- [48] L. Mosecker, D.T. Pierce, A. Schwedt, M. Beighmohamadi, J. Mayer, W. Bleck, J.E. Wittig, Temperature effect on deformation mechanisms and mechanical properties of a high manganese C+N alloyed austenitic stainless steel, *Mater. Sci. Eng. A* 642 (2015) 71–83.
- [49] P.S. Follansbee, U.F. Kocks, A constitutive description of the deformation of copper based on the use of mechanical threshold stress as an internal state variable, *Acta Metall.* 36 (1988) 81–93.
- [50] S. Asgari, E. El-Danaf, S. Kalidindi, R. Doherty, Strain hardening regimes and microstructural evolution during large strain compression of low stacking fault energy FCC alloys that form deformation twins, *Metall. Trans. A* 28 (1997) 1781–1795.
- [51] R. Abbaschian, L. Abbaschian, R.E. Reed-Hill, *Physical Metallurgy Principles*, in: H. Gowan (Ed.), 4 Ed., Cengage Learning, Stamford, 2009.
- [52] D. Kuhlmann-Wilsdorf, Energy minimization of dislocations in low-energy dislocation structures, *Phys. Stat. Sol. A* 104 (1987) 121–144.
- [53] D. Kuhlmann-Wilsdorf, N. Hansen, Theory of work-hardening applied to stages III and IV, *Metall. Trans. A* 20 (1989) 2393–2397.
- [54] D. Kuhlmann-Wilsdorf, H.G.F. Wilsdorf, J.A. Wert, LEDS theory of work hardening stages and “planar” versus “distributed glide, *Scr. Metall.* 31 (1994) 729–734.
- [55] O. Bouaziz, N. Guelton, Modeling of TWIP effect on work-hardening, *Mater. Sci. Eng. A* 319–321 (2001) 246–249.
- [56] A.D. Rollet, U.F. Kocks, A review of the stages of work hardening, *Sol. St. Phen.* 35 (1994) 1–18.
- [57] H. Mecking, U.F. Kocks, Kinetics of flow and strain-hardening, *Acta Metall.* 29 (1981) 1865–1875.
- [58] Y. Tomota, M. Strum, J.W. Morris, Microstructural dependence of Fe–high Mn tensile behavior, *Metall. Trans. A* 17 (1986) 537–547.
- [59] S.R. Kalidindi, A.A. Salem, R.D. Doherty, Role of deformation twinning on strain hardening in cubic and hexagonal polycrystalline metals, *Adv. Eng. Mater.* 5 (2003) 229–232.
- [60] I. Gutiérrez-Urrutia, Raabe, Multistage strain hardening through dislocation substructure and twinning in a high strength and ductile weight-reduced Fe–Mn–Al–C steel, *Acta Mater.* 60 (2012) 5791–5802.
- [61] G. Dini, A. Najafizadeh, R. Ueji, S.M. Monir-Vaghefi, Tensile deformation behavior of high manganese austenitic steel: the role of grain size, *Mater. Des.* 31 (2010) 3395–3402.